




AUGMENTING PHYSICS-BASED MODELS IN ICME WITH MACHINE LEARNING AND UNCERTAINTY QUANTIFICATION

Surrogate Modeling of Viscoplasticity in Steels: Application to Thermal, Irradiation Creep and Transient Loading in HT-9 Cladding

AARON E. TALLMAN ^{1,2} M. ARUL KUMAR,¹
CHRISTOPHER MATTHEWS,¹ and LAURENT CAPOLUNGO¹1.—Materials Science and Technology Division, Los Alamos National Laboratory, Los Alamos, NM, USA. 2.—e-mail: aaronetallman@gmail.com

The use of structural metals in extreme environments relies both on the characterization of the mechanical response and microstructure changes in service and on modeling predictions. Data scarcity creates a need for predictive constitutive models that can be used in regimes outside calibration domains. While crystal plasticity models can be applied to non-monotonic loads and complex environments, their computational cost typically prohibits use at the level of an engineering structure. As an alternative, the present study introduces a surrogate constitutive model derived from crystal-plasticity predictions of the mechanical response of HT9 subjected to irradiation, stresses and temperatures. The surrogate law is then tested in the cases of uniaxial straining, stress cycling, thermal cycling and thermal ramping. Finally, using this constitutive relationship, finite element simulations of a pressurized tube subjected to a stress and thermal transients are performed and analyzed.

INTRODUCTION

The use of metals under extreme environments (e.g., nuclear), for which testing is necessarily limited/complex, stresses the need for engineering-scale models that predict the mechanical response and microstructure evolution of materials in conditions largely departing from those under which a constitutive model can be fully calibrated. For example, in many of the advanced nuclear reactors currently being developed,¹ accident scenarios involving cladding failure generally result from high temperature excursions,^{2–5} heightened chemical attacks via fuel-cladding chemical interaction⁶ or corrosion.^{7,8} Such accident scenario initiators are difficult to reproduce in a laboratory environment, and the number of tests simultaneously subjecting samples to temperature, multi-axial stresses and irradiation is limited by cost and time. Consequently, constitutive models are relied upon to predict cladding strain evolution.⁹ The accuracy of

these models is exceedingly important; underestimations in cladding strain would lead to designs promoting premature cladding failure, while overestimations result in increased safety margins and decreased reactor profitability.

Given the complex environment the cladding material is subjected to, i.e., temperature, stress, irradiation dose, dose rates and data scarcity (i.e., irradiated samples), a simple empirical model fit to the experimental data will likely be of limited applicability beyond the regimes in which the experimental data were acquired.¹⁰ Rather, a constitutive model tracking the activation of distinct deformation modes and the state of the microstructure is preferred.^{9,11,12} In this regard, mechanistic constitutive models have recently been developed to predict the high-temperature viscoplastic response of many cladding materials (e.g., stainless steels, zircaloy, etc.), including HT-9.^{9,13–17} In practice, the direct use of crystal plasticity-based polycrystal models for structural applications can be computationally cost prohibitive.^{18–21} Instead, multiscale approaches have been proposed.^{19,22–29} Typically, this consists of polycrystal codes (either full-field^{17,19,20,22} or mean-

field methods³⁰) directly embedded within a finite element (FE) solver.³⁰ The latter is then used to simulate the response of a structure. As a numerically efficient alternative, it has been proposed to pass surrogate models (SMs) to the FE solver. SMs are derived from databases of expected mechanical responses populated from crystal plasticity-based polycrystal simulations. They can adopt many forms: look-up tables, Fourier coefficient databases³¹ or interpolative or regression models.³² Recently, a SM was proposed to predict the primary and secondary creep response of 316H.³² This polynomial regression-based model should acceptably reproduce predictions of both mechanical response and dislocation density evolutions as derived from polycrystal models. However, the range of applicability (temperatures from 800 K to 1000 K and stresses of 120 MPa to 300 MPa) was a limitation.

In the present study, a previously developed polycrystal constitutive model for HT-9 alloy is used to derive a SM. The polycrystal constitutive model uses the Visco-Plastic Self Consistent (VPSC) framework.⁹ It is used to populate a database describing the evolution of the equivalent plastic strain rate and dislocation densities inside cells and cell walls as a function of imposed von Mises stress, temperature, irradiation dose rate, current dislocation content and accumulated plastic strain during creep. Using this database which contains > 40,000 creep simulations, a new approach is proposed whereby multiple polynomial regression models are tiled to generate a surrogate constitutive model spanning a large domain of temperatures [600, 1100 K], stresses [0.1, 300 MPa] and dose rates [1×10^{-9} , 1×10^{-6} dpa/s]. The SM is first validated against a new set of VPSC creep simulations over temperatures from 600 K to 1100 K and stresses from 0.1 MPa to 300 MPa. Furthermore, the SM is assessed for four cases in which it was not calibrated: uniaxial loading, stress cycling, temperature cycling and temperature ramp under constant stress. It is found that the SM performs remarkably well in stress cycling conditions but that the predictions deteriorate—albeit while capturing the evolutions of defect content and strain rates—in thermal cycling conditions and under fast temperature ramps.

Finally, the SM is used to predict the mechanical response under transient conditions and deformation of pressurized tubes subjected to a slow pressure and temperature ramp. From the engineering standpoint, these FE simulations aim to capture the experimentally measured deformation behaviors of HT9 alloy under simulated transient tests at the Fuel Cladding Transient Test (FCTT) system³³ in which tubes were internally pressurized and heated at a constant rate until the specimen failed.³⁴ It is shown that the rate of reduction in tube wall thickness strongly correlated with the imposed internal pressure and temperature ramp.

METHODS

Crystal Plasticity-Based Mechanistic Constitutive Modeling

The database of polycrystal mechanical response was generated using the VPSC framework, whereby the individual viscoplastic response of each grain is described with a recently proposed crystal plasticity-based model.⁹ For the sake of completeness, some of the most important elements of this constitutive model are described in what follows.

Using a small strain formulation, the total creep rate is expressed as the sum of three contributions:

$$\dot{\epsilon}^p = \dot{\epsilon}^d + \dot{\epsilon}^c + \dot{\epsilon}^{\text{coble}} \quad (1)$$

where $\dot{\epsilon}^d$, $\dot{\epsilon}^c$ and $\dot{\epsilon}^{\text{coble}}$ refer to the plastic strain rate due to dislocation glide, dislocation climb and Coble creep, respectively. These deformation mechanisms depend differently on the temperature, stress and internal state. The strain rates due to glide and climb of dislocations are written as the sum of the mean shear/climb rates contributed by all active slip systems in a given grain, i.e.,

$$\dot{\epsilon}^d = \sum_s m_{ij}^s \bar{\gamma}^s \text{ and } \dot{\epsilon}^c = \sum_s c_{ij}^s \bar{\beta}^s \quad (2)$$

Here, m^s is the symmetric part of the Schmid tensor, $c^s = (b^s \otimes b^s)$ is the climb tensor for edge dislocations,³⁵ and $\bar{\gamma}^s$ and $\bar{\beta}^s$ denote the mean shear and mean climb rates in slip system s of the grain, respectively. This constitutive model takes into account the distribution of internal stresses inside a grain resulting from the presence of dislocations. These internal stresses are used to calculate the average shear/climb rates within each grain as in Refs. 36 and 37. At individual sub-material points (i.e., sub-volume within a material point), the glide and climb rates are explicitly connected to the dislocation density using Orowan-type equations:

$$\dot{\gamma}^s = \rho_{\text{cell}}^s b^s V^s \cdot \text{sign}(\tau^s) \quad \text{and} \quad \dot{\beta}^s = \rho_{\text{cell,edge}}^s b^s V_{\text{climb}}^s, \quad (3)$$

where $\dot{\gamma}^s$ and $\dot{\beta}^s$ are the shear and climb rate at a sub-material point, respectively. ρ_{cell}^s and $\rho_{\text{cell,edge}}^s$ are the total dislocation density in the cells and edge-dislocation density, respectively. b^s is the Burgers vector, and V^s and V_{climb}^s are the mean dislocation glide and climb velocity, respectively. The dislocation glide velocity is calculated using the mean spacing between obstacles (dislocation mean free path, λ^s) and the time a dislocation spends traveling between obstacles (= waiting time at obstacles (t_w^s) + travel time within the interspacing (t_t^s)):

$$V^s = \frac{\lambda^s}{t_w^s + t_t^s} \quad (4)$$

The mean dislocation interspacing associated with dislocation–dislocation interactions is written as,³⁸

$$\frac{1}{\lambda^s} = \sqrt{\sum_s \bar{\alpha}^{ss'} \rho_{\text{cell}}^{s'}}. \quad (5)$$

where $\bar{\alpha}^{ss'}$ refers to the latent hardening matrix. The traveling time is given by t_t^s . Following a Kocks-type activation energy law,³⁹ the waiting time is written as:

$$t_w^s = \begin{cases} \frac{1}{\nu^s} \exp\left(\frac{\Delta G_0}{kT} \left(1 - \left(\frac{|\tau_{\text{eff}}^s|}{\tau_c^s}\right)^p\right)^q\right) & \text{if } |\tau_{\text{eff}}^s| < \tau_c^s \\ 0 & \text{if } |\tau_{\text{eff}}^s| \geq \tau_c^s \end{cases} \quad (6)$$

where ΔG_0 is the thermal activation energy without any external stress. k is the Boltzmann constant. T is the absolute temperature. p ($0 < p \leq 1$) and q ($1 < q \leq 2$) are the exponent parameters. $\nu^s = \chi_e C_s / \lambda^s$ is the attack frequency, which is a function of mean spacing among obstacles λ^s , shear wave velocity C_s and entropy factor χ_e (~ 1.0). τ_c^s refers to the critical resolved shear stress (CRSS), which accounts for the hardening due to (1) lattice friction without the presence of solutes, (2) second-phase precipitates and (3) dislocation interactions with cell-wall structure. τ_{eff}^s represents the effective driving stress available for a mobile dislocation to overcome the barriers. Dislocation densities evolve (depleting under creep conditions) as dislocations interact via generation, dynamic recovery and trapping at the cell wall. For more details, refer to the supplementary material and Wen et al.⁹

The climb velocity V_{climb}^s depends on the imbalance between vacancies and interstitials being trapped by the dislocation. The climb velocity is written as

$$\begin{aligned} \bar{V}_{\text{climb}}^s &= \frac{\Omega}{b} I^s \\ &= \frac{\Omega}{b} \left(z_i^s D_i c_i^{\text{sat}} - z_v^s D_v \left(c_v^{\text{sat}} - c_v^{\text{th}} \exp\left(\frac{\Omega \bar{\tau}_{\text{climb}}^s}{kT}\right) \right) \right) \end{aligned} \quad (7)$$

where $\Omega \approx b^3$ represents the atomic volume. $\bar{\tau}_{\text{climb}}^s$ is the effective resolved climb stress. D_i and D_v denote the diffusivity for interstitial and vacancy. z_i^s and z_v^s denote the dislocation capture efficiencies for interstitial and vacancy. c_v^{th} is the thermal equilibrium vacancy concentration. c_i^{sat} and c_v^{sat} are the saturation concentrations for interstitial and vacancy, respectively, under combined thermal and irradiation conditions. The saturation densities at equilibrium can be written as

$$\begin{aligned} c_i^{\text{sat}} &= \frac{K_0}{\sum_s (z_i^s \rho_{\text{cell}}^s) D_i} \quad \text{and} \\ c_v^{\text{sat}} &= \frac{K_0 + \sum_s \left(z_v^s \rho_{\text{cell}}^s \exp\left(\frac{\Omega \bar{\tau}_{\text{climb}}^s}{kT}\right) \right) D_v c_v^{\text{th}}}{\sum_s (z_v^s \rho_{\text{cell}}^s) D_v} \end{aligned} \quad (8)$$

where K_0 is the defect-pair creation rate per unit volume, and it is calculated by multiplying the imposed irradiation dpa rate with the defect creation efficiency ($\sim 10\%$ to 40%).

Coble creep occurs as a consequence of the diffusion of point defects within grain boundaries.⁴⁰ In the VPSC model, grain boundaries are not represented explicitly, and the grain boundary-related material properties are not known for the studied steel system. Thus, the coble creep is re-written in a simple form to capture the stress and temperature dependence as

$$\begin{aligned} \dot{\epsilon}_{ij}^{\text{coble}} &= \alpha \frac{\delta'}{d^3} \frac{\Omega S_{ij}}{kT} D_0^{\text{GB}} \exp\left(-\frac{Q_m^{\text{GB}} + Q_f^{\text{GB}}}{kT}\right) \\ &= \frac{A^{\text{coble}} S_{ij}}{T} \exp\left(-\frac{Q_{\text{gb}}}{kT}\right), \end{aligned} \quad (9)$$

where α is the geometric per-factor. δ' and d represent the grain boundary width and average grain size (diameter). Ω is the atomic volume. D_0^{GB} is the vacancy diffusion constant at the grain boundary. Q_f^{GB} and Q_m^{GB} denote the vacancy formation energy and the activation energy for the diffusion along the grain boundary, respectively. S_{ij} is the component of the deviatoric stress tensor. In the simplified relation, $A^{\text{coble}} = \alpha \frac{\delta' \Omega}{d^3 k} D_0^{\text{GB}}$ and $Q_{\text{gb}} = Q_m^{\text{GB}} + Q_f^{\text{GB}}$ are effective parameters that represent all point defects.

The VPSC model was calibrated and validated against the experimental literature⁴¹ as reported in Wen et al.⁹ Thermal creep data at temperatures from 753 K to 873 K and stresses from 9 MPa to 173 MPa were compared in Fig. 2 of Ref. 9. Irradiation creep data at $8.0 \cdot 10^{-7}$ dpa s^{-1} were compared in Fig. 5 of Ref. 9. In this work, the material parameters determined in Ref. 9 are used in all simulations.

Database Generation

Polycrystal simulations (42,121 in training, 1609 in testing) are used to generate a compact database storing the accumulated effective plastic strain, equivalent plastic strain rate, von Mises stress, dose rate and average dislocation density in the cells and in cell walls during creep simulations. Note that the use of average dislocation density per slip system and per grain, $\bar{\rho}_{\text{cell}}$, $\bar{\rho}_W$, rather than that of dislocation densities on each slip system s (ρ_{cell}^s , ρ_W^s) and in each grain significantly reduces the size of the database. The database therefore aims to capture the relationship between inputs, $[\bar{\epsilon}_{\text{vm}}, \bar{\rho}_{\text{cell}}, \bar{\rho}_W, T, \bar{\sigma}_{\text{vm}}, \dot{\phi}]$, and the isotropic homogeneous rates, $\dot{\epsilon}_{\text{vm}}$, $\dot{\rho}_{\text{cell}}$ and $\dot{\rho}_W$ —these define the outputs of the SM. Polynomial regression is used to relate the inputs and outputs. However, all inputs and outputs are transformed/mapped to linearize the transformed input–output relationships.

The database is assembled from simple creep test simulations with varying inputs, the objective being to capture the effects of initial dislocation concentrations on each slip system ($\rho_{\text{cell},0}^s$, $\rho_{\text{W},0}^s$), temperature, effective applied stress ($\bar{\sigma}_{\text{vm}}$) and dose rate ($\dot{\phi}$) on the strain rate and dislocation density evolution. The ranges of these initial conditions are shown in Table I. A systematic random sampling procedure is used to sample the given ranges.⁴² A randomly textured set of 50 grain orientations is used to represent the polycrystalline aggregate for all simulations, consistent with heat-treated HT-9 used in nuclear energy applications.⁴³ For HT-9 alloy, $\{110\}\langle 111 \rangle$ and $\{112\}\langle 111 \rangle$ systems are considered for both the dislocation glide and climb. All slip systems have initially equal dislocation densities. Principal stress directions are chosen at random for each simulation (i.e., all simulations subjected the sample to multi-axial loading). The simulations are stress controlled, and the time step size is adjusted automatically to maintain a reasonable strain increment. Simulations continued to maximum strain values between 0.005 and 0.5, depending on the simulation.

The constitutive model also provides the relative contribution of each deformation mechanism (i.e., dislocation glide, climb and Coble creep). The variation in the dominant mechanisms across the operating condition ranges of interest was examined; a set of 500 simulations is plotted in terms of T and $\bar{\sigma}_{\text{vm}}$ and grouped by dominant deformation mechanism(s) in Fig. 1. The zones were determined in terms of the contributions of each mechanism to total creep strain, using zone boundaries as shown in the ternary diagram in Fig. 1. When the most dominant mechanism accounted for $< 80\%$ of the strain, more than one mechanism was used to label the category. As an example, the evolution of the contribution of the different plastic deformation mechanisms at 29.6 MPa and 792.7 K is shown in the top right of Fig. 1. Dislocation glide is shown to be dominant over most of the operating conditions. Glide is expected to dominate within 10% of yield stress (as seen in an Ashby map of ferritic creep resistant steel⁴⁴), which is most of the target domain given that yield strength of HT-9 ranges from 200 MPa to 550 MPa for a temperature range of 300 K to 1000 K.^{45,46} At lower $\bar{\sigma}_{\text{vm}}$ and T , climb and Coble creep become the dominant deformation mechanisms.

Surrogate Model Formulation

Assuming an isotropic plastic response, the SM relates the overall plastic strain rate tensor to the equivalent plastic strain rate via a Prandtl–Reuss flow rule, i.e.,

$$\dot{\epsilon}_{ij} = \dot{\epsilon}_{\text{vm}} \frac{3}{2} \frac{S_{ij}}{\bar{\sigma}_{\text{vm}}} \quad (10)$$

$\bar{\sigma}_{\text{vm}} = \sqrt{\frac{3}{2} S_{ij} S_{ij}}$ denotes the von Mises stress. Given the broad operating conditions considered, the newly developed SM relies on the use of multiple polynomial regression models (here called ‘tiles’). Within each tile, defined by a subdomain (i.e., temperature and stress ranges), the SM is defined as a Legendre polynomial expansion. $P_i(x)$ denotes the polynomial of degree i , evaluated for input x , where the range of x has been normalized to the $[-1, 1]$ interval. The regression formulation includes polynomial terms of each mapped/transformed input parameter and all interaction terms thereof, i.e.,

$$\begin{aligned} \dot{\epsilon}_{\text{vm}}^{**} \sim & \sum_{0 \leq i,j,k,l,m,n \leq N_{\text{deg}}} \alpha_{\epsilon}^{ijklmn} P^i(\bar{\rho}_{\text{cell}}^*) P^j(\bar{\rho}_{\text{w}}^*) P^k(T^*) \\ & P^l(\sigma_{\text{vm}}^*) P^m(\epsilon_{\text{vm}}^*) P^n(\dot{\phi}^*) \end{aligned} \quad (11)$$

$$\begin{aligned} \dot{\rho}_{\text{cell}}^{**} \sim & \sum_{0 \leq i,j,k,l,m,n \leq N_{\text{deg}}} \alpha_{\rho_{\text{cell}}}^{ijklmn} P^i(\bar{\rho}_{\text{cell}}^*) P^j(\bar{\rho}_{\text{w}}^*) P^k(T^*) \\ & P^l(\sigma_{\text{vm}}^*) P^m(\epsilon_{\text{vm}}^*) P^n(\dot{\phi}^*) \end{aligned} \quad (12)$$

$$\begin{aligned} \dot{\rho}_{\text{w}}^{**} \sim & \sum_{0 \leq i,j,k,l,m,n \leq N_{\text{deg}}} \alpha_{\rho_{\text{w}}}^{ijklmn} P^i(\bar{\rho}_{\text{cell}}^*) P^j(\bar{\rho}_{\text{w}}^*) P^k(T^*) \\ & P^l(\sigma_{\text{vm}}^*) P^m(\epsilon_{\text{vm}}^*) P^n(\dot{\phi}^*) \end{aligned} \quad (13)$$

where N_{deg} is the maximum degree of the polynomial to be used in the model; $\alpha_{\epsilon}^{ijklmn}$ are the regression coefficients for each term. When $N_{\text{deg}} = 2$, $\alpha_{\epsilon}^{ijklmn}$ contains $(N_{\text{deg}} + 1)^{N_{\text{inputs}}} = 729$ values. Symbols * and ** denote the fact that the input or output has been transformed/mapped. The transformations must satisfy analytical constraints and should reflect observed trends. The transformations must be bijective. They can also enforce physical bounds (e.g., non-negative dislocation densities).

Table I. Bounds of the polycrystal simulation input domain over which the database of constitutive responses is gathered

Parameter	$\rho_{\text{cell}}^s (\text{m}^{-2})$	$\rho_{\text{W}}^s (\text{m}^{-2})$	$\sigma_{\text{vm}} (\text{MPa})$	$T (\text{K})$	$\dot{\phi} (\text{dpa/s})$
[min, max]	$[1 \times 10^{12}, 7 \times 10^{12}]$	$[8 \times 10^{12}, 12 \times 10^{12}]$	$[0.1, 300]$	$[600, 1100]$	$[1 \times 10^{-9}, 1 \times 10^{-6}]$

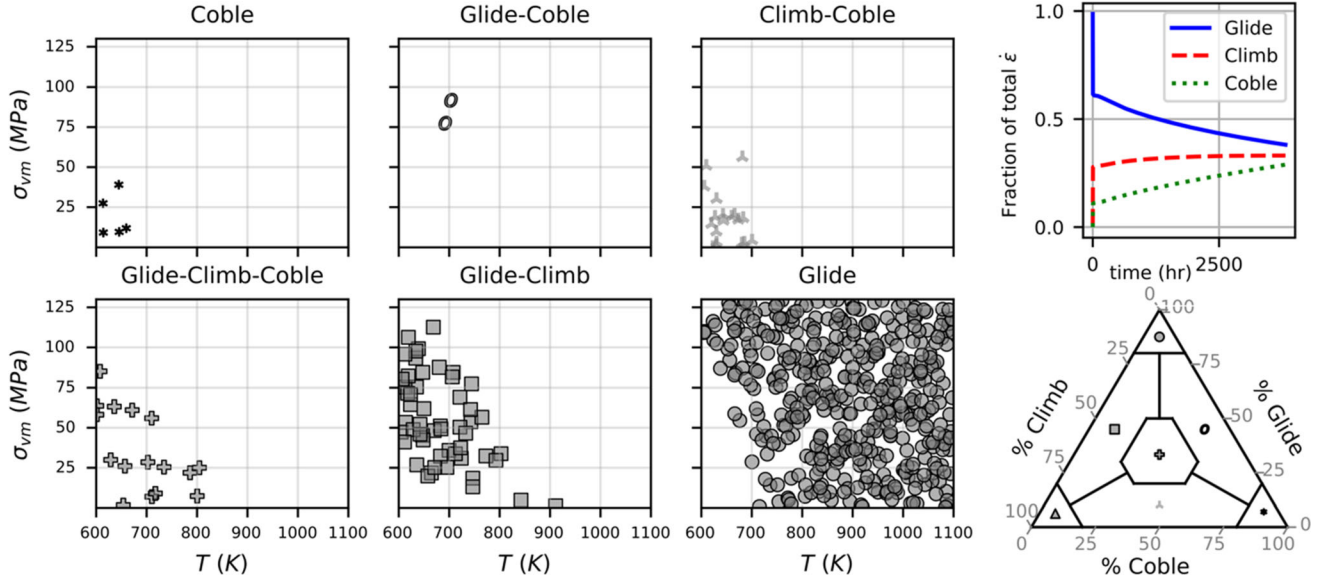


Fig. 1. Scatter plots of constitutive model simulations of HT-9 thermal and irradiation creep, grouped by the dominant deformation mechanism(s) reported by VPSC. The dominant mechanism is evaluated as the largest contribution to the first 0.5% strain. An example of the relative contribution to the strain of each mechanism as a function of time is shown in the top right (at 29.6 MPa and 792.7 K). A ternary diagram distinguishes the boundaries used to divide the various simulations into categories in terms of percent of total accumulated strain.

These transformations are necessary because strain rates do not typically have a linear dependence on boundary conditions T , $\dot{\phi}$ and $\bar{\sigma}_{vm}$, or the microstructure state variables $\bar{\rho}_{cell}$ and $\bar{\rho}_w$, whereas polynomial regression will only fit well when inputs and outputs scale in near-linear fashion. For instance, the depletion of dislocations during creep supported a near-logarithmic shaped transform of the accumulated effective strain to allow a polynomial fit, i.e., $f(\dot{\epsilon}_{vm}) \propto \log(\dot{\epsilon}_{vm} + m) = \dot{\epsilon}_{vm}^*$, where m is a constant parameter. These transformations are applied prior to normalizing to the interval $[-1, 1]$ for generating Legendre polynomial terms.

These mapping functions use a constant, m , to modify the transformation. The mappings applied to the inputs (e.g., $\dot{\phi}^* = h(\dot{\phi})$) and outputs, e.g., $\dot{\epsilon}_{vm}^* = f(\dot{\epsilon}_{vm})$, are determined uniquely for different tiles and are included in supplementary tables S1–S3. To allow for both negative and positive rates, a piecewise mapping is used, i.e.,

$$\dot{\rho}_{cell}^* = \begin{cases} \ln\left(\frac{-\dot{\rho}_{cell}}{\bar{\rho}_{cell}} + m\right) & \text{if } z > 0, \\ \ln\left(-\frac{m^2}{\frac{\dot{\rho}_{cell}}{\bar{\rho}_{cell}} - m}\right) & \text{if } z \leq 0 \end{cases} \quad (14)$$

where m is a modifier used to tune the mapping.

The range of stress and temperature was subdivided into 15 overlapping tiles to isolate regions dominated by different deformation mechanisms. These tiles can be visualized in Fig. 2a by using a unique crosshatching for each. The tiles include unique T limits $([600, 825], [708.3, 991.7], [875, 1100]K)$ and $\bar{\sigma}_{vm}$ limits $([0.1, 81.1], [39.1, 141.1], [99.1, 201], [159, 261], [219, 300]MPa)$. Figure 2b shows the simulations from Fig. 1

superimposed with the tile limits. The adjacent ternary diagram defines the different creep regimes in percent accumulated strain contributed by each deformation mechanism. The tile layout is chosen to match the deformation mechanism domains. Optimization of the tile placement is not pursued in this work.

Finally, the values of the regression coefficients, α_e^{ijklmn} , $\alpha_{\rho_{cell}}^{ijklmn}$, α_w^{ijklmn} , are determined using the reduced database, mappings and subdomains. The SM was made continuously differentiable across tiles. Within tile overlaps, multiple strain rates were combined to obtain a single strain rate using weights to enforce smoothness. A sigmoid function was selected to define the weights assigned to each model covering the overlapped region, i.e.,

$$w_1 = \frac{1}{1 + \exp\left(\frac{4v}{v^2 - 1}\right)}, w_2 = 1 - w_1 \quad (15)$$

$$\dot{\epsilon} = w_1 \dot{\epsilon}_1 + w_2 \dot{\epsilon}_2 \quad (16)$$

where the value of $v \in (-1, 1)$ is determined from the boundaries of the overlap in terms of the input dimension being tiled (i.e., temperature or stress). The value is determined,

$$v = \frac{2(x - x_{min})}{x_{max} - x_{min}} - 1 \quad (17)$$

where the x values correspond to the input value of the tiling overlap (either T or σ_{vm}). Notably, in the case of overlapping in two dimensions at once, this weighted summing can be repeated with otherwise no change in procedure.

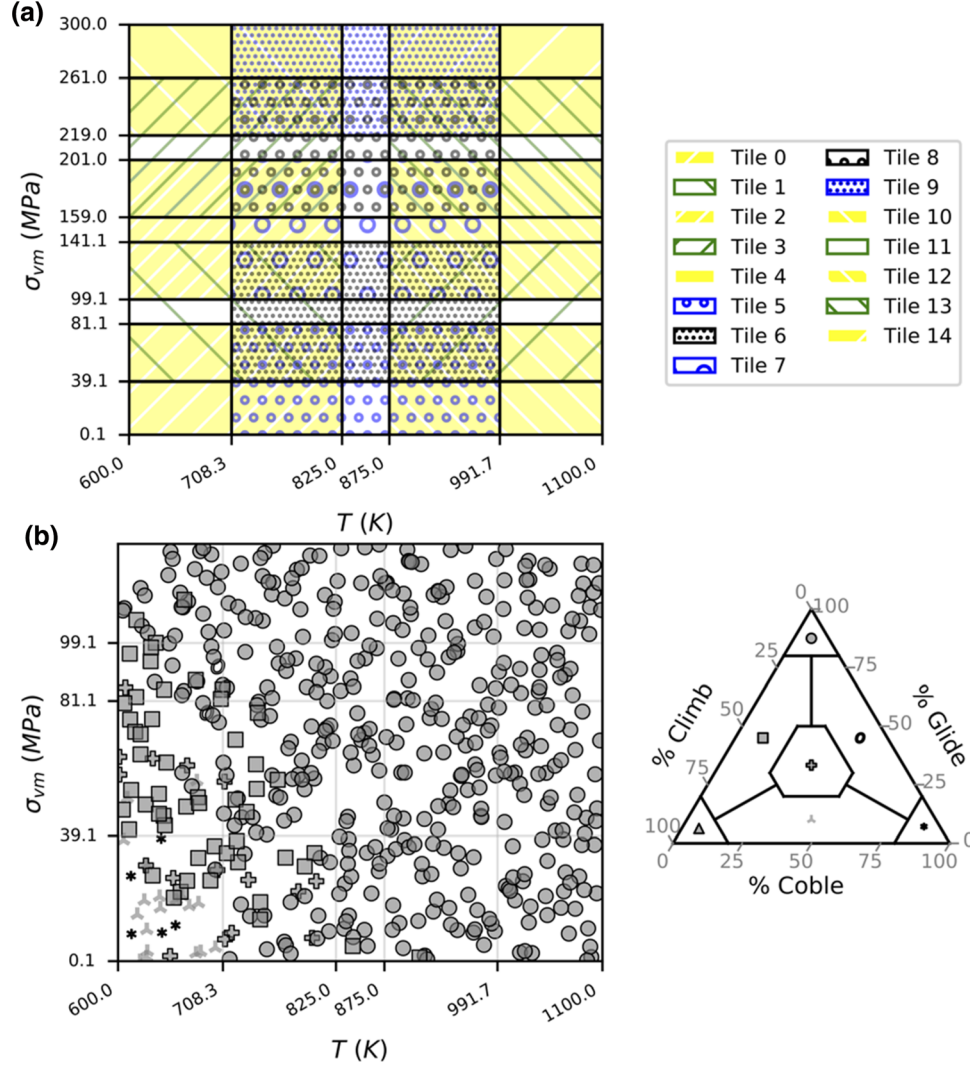


Fig. 2. (a) Layout of the overlapping tile subdomains. (b) The categories of the dominant mechanism, defined in terms of percentage of total creep strain contributed by each of the mechanisms shown in the ternary legend, superimposed on the tile subdomains for stresses < 130 MPa.

SURROGATE MODELING PERFORMANCE

One thousand three hundred ten creep tests starting from various initial conditions are performed to assess the accuracy of SM across the target domain. For example, two cases are shown in Fig. 3. These cases consider the following stress, temperature and irradiation conditions: (a) $\bar{\sigma}_{vm} = 128.7$ MPa, $T = 789$ K, $\dot{\phi} = 3.82 \times 10^{-8}$ dpa/s and (b) $\bar{\sigma}_{vm} = 50.4$ MPa, $T = 607$ K, $\dot{\phi} = 4.83 \times 10^{-7}$ dpa/s. Case (a) is an example of glide-dominated creep, and case (b) is an example of increased climb and Coble creep. The VPSC simulations (red) and the SM predictions (blue) are shown for the accumulated effective strain and the dislocation density evolution in cells and cell walls. As shown, in these the SM reproduces VPSC predictions in terms of both the trends and absolute values of the strain rate and dislocation density evolutions. We use the mean relative squared error (MSRE) of the ϵ_{vm}

values at each time step in the creep simulation to quantify the accuracy of the SM. The MSRE is expressed as

$$MSRE = \frac{1}{n_{ts}} \sum_i \left(\frac{\epsilon_{vm,i}^{SM} - \epsilon_{vm,i}^{VPSC}}{\epsilon_{vm,i}^{VPSC}} \right)^2, \quad (18)$$

where i refers to the i -th timestep in the simulation and n_{ts} is the number of timesteps in the simulation. The two cases shown have MSRE values of 7.8×10^{-3} and 1.8×10^{-2} , respectively.

More comprehensively, the distribution of MSRE was assessed across the entire target domain (all 15 tiles), featuring strain rates from 10^{-12} to 10^2 s $^{-1}$. These are shown in Fig. 4a. The MSRE of the tiled SM predictions is generally below 1×10^{-1} within the outlined region (see (b)). One notes discrepancies under the highest and lowest stresses. The highest MSRE values coincide with regions with very high and very low strain rates.

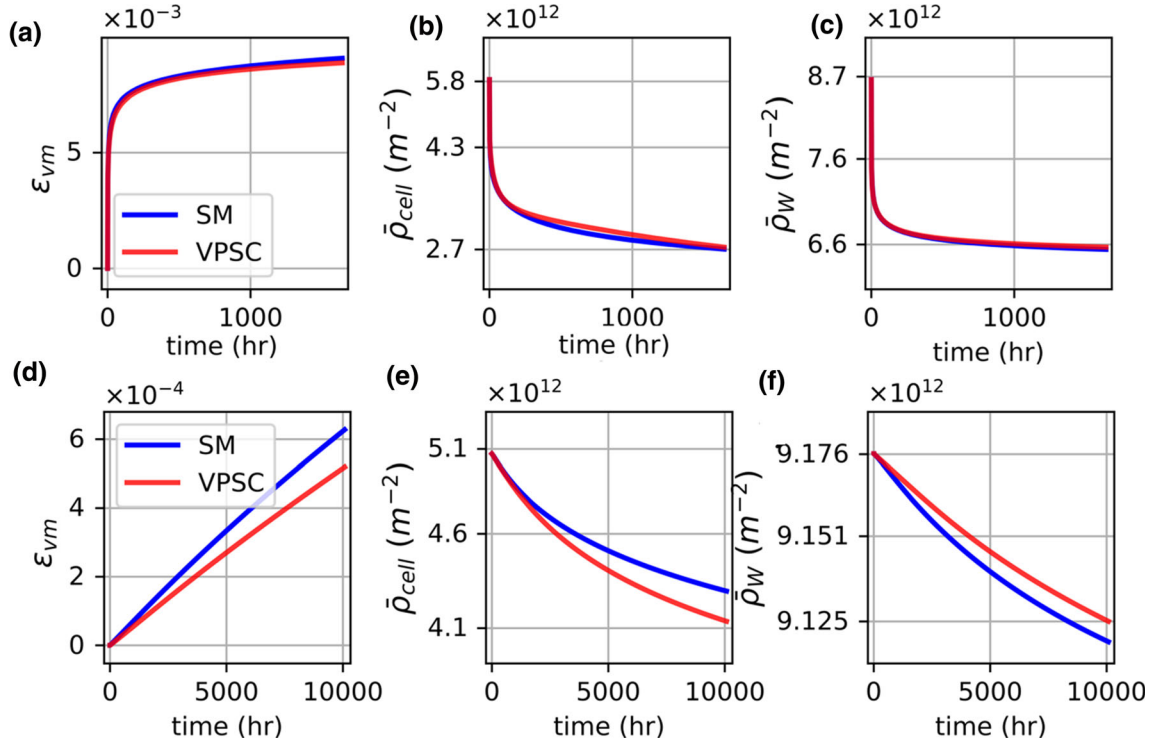


Fig. 3. Validation of the developed nine-tile SM against reserved VPSC simulations of ϵ_{vm} , $\bar{\rho}_{cell}$ and $\bar{\rho}_w$ over time. (a–c) Initial values: $[\bar{\rho}_{cell,0} = 5.85 \times 10^{12} m^{-2}, \bar{\rho}_{w,0} = 8.66 \times 10^{12} m^{-2}, \bar{\sigma}_{vm} = 128.7 MPa, T = 789K, \dot{\phi} = 3.82 \times 10^{-8} dpa/s]$; (d–f) initial values: $[\bar{\rho}_{cell,0} = 5.07 \times 10^{12} m^{-2}, \bar{\rho}_{w,0} = 9.18 \times 10^{12} m^{-2}, \bar{\sigma}_{vm} = 50.4 MPa, T = 607K, \dot{\phi} = 4.83 \times 10^{-7} dpa/s]$.

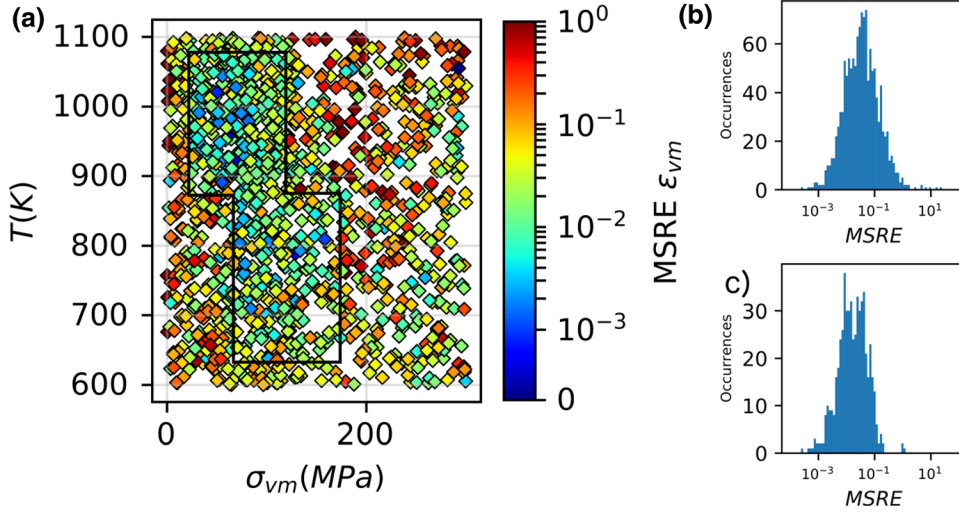


Fig. 4. (a, b) Creep simulations (1310) predicted using the 15-tile SM over the T and σ domain. (c) The MSRE within the outlined region.

Beyond the previous validation, the accuracy of the SM in different cases relevant to actual operating conditions is investigated. Four of these cases are included: (1) displacement-control uniaxial tension, (2) stress cycling, (3) thermal cycling and (4) temperature ramp. These cases that depart from the SM training database are subject to inaccuracies arising from differences between training and

testing. In all cases, the initial cell and cell-wall dislocation densities were assumed to be $4 \times 10^{12} m^{-2}$ and $10 \times 10^{12} m^{-2}$, respectively. The imposed dose rate was fixed for all the cases as $8 \times 10^{-7} dpa s^{-1}$.

Strain hardening predicted by the SM from only stress relaxation data is compared with the VPSC model. A strain rate of $1 \times 10^{-4} s^{-1}$ is imposed at

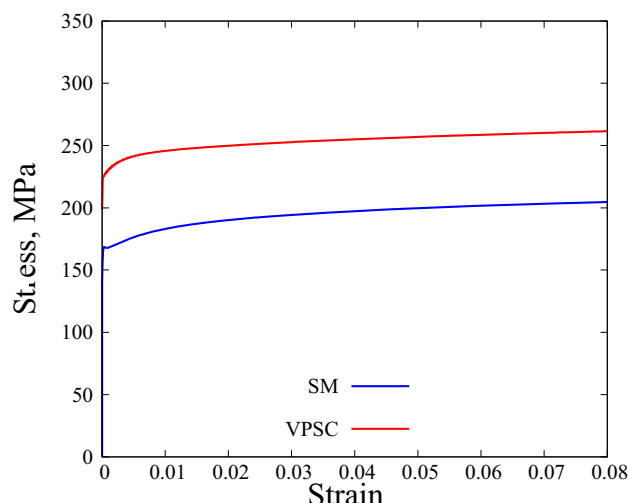


Fig. 5. SM and VPSC model predictions of the stress-strain response of HT9 alloy subjected to monotonic uniaxial loading at 973 K with an imposed strain rate of 10^{-4} s^{-1} . The initial cell and cell-wall dislocation densities are $4 \times 10^{12} \text{ m}^{-2}$ and $10 \times 10^{12} \text{ m}^{-2}$, respectively.

973 K to simulate a uniaxial loading. As shown in Fig. 5, the SM qualitatively reproduces the hardening curve as predicted by the VPSC model. Note, however, that the SM significantly underestimates the initial yield point of the material. The match in mechanical response is for the most part due to the fact that the SM can track the increase in dislocation content during loading conditions under which the model was not trained.

For the case of stress cycling, constant effective stress of 80 MPa was held for 600 s after which stress cycling was introduced with an amplitude and period of 20 MPa and 3600 s, respectively, as shown in Fig. 6a. The stress cycle simulations were performed at a constant temperature of 900 K. The evolutions of creep rate and cell and cell wall dislocation densities as predicted by VPSC and the SM are shown in Fig. 6b, c and d, respectively. During the initial constant stress regime and under the stress cycle, the SM predictions agree with the VPSC model predictions. The tracking of dislocation densities, for which evolution is opposite to that in the monotonic loading case, allows the SM to correctly predict the transient behavior under stress cycles.

Third, a thermal cycle was simulated in which a temperature of 850 K was held constant for the first 600 s and then varied with an amplitude and period of 40 K and 3600 s, respectively; see Fig. 6e. Both the SM and the mechanistic VPSC model predictions are shown for a constant stress of 100 MPa in terms of the effective strain rate. During the initial constant temperature regime, as expected, the SM predicted a decrease in effective creep rate with

time and matches well with the VPSC model predictions. Later under the thermal cycle, the evolution of the creep rate as predicted by the SM follows the imposed temperature profile and matches the trends of VPSC model predictions. However, the effective strain rate is far more sensitive to temperature evolutions in the SM compared to predictions from the VPSC model.

Lastly, the SM was used to simulate the transient because of a temperature ramp under constant stress. To impose the transient conditions, a temperature of 700 K was held constant for 600 s and ramped up from 700 K to 1000 K with different rates, as schematically shown in Fig. 6i. Three different temperature rates were used (0.01 K/s, 0.1 K/s and 1.0 K/s). As shown in Fig. 6j, k and l, the SM qualitatively captures the effect of temperature ramp rates on the strain rate and dislocation density evolution as predicted by the VPSC model. That is, the increase in strain rate with increasing temperature ramp rates qualitatively agrees with VPSC predictions. However, the accuracy of the SM is found to deteriorate significantly with an increase in temperature ramp rate.

In summary, the four cases considered clearly show that while the SM can acceptably predict trends (i.e., strain rate and dislocation density evolutions) in conditions far removed from those used to generate the database from which it is derived, its accuracy is limited by a lack of appropriate sensitivity to temperature changes. Transients associated with mechanical loading (i.e., strain ramp, stress cycles) are therefore accurately predicted by the SM while those associated with thermal loading are not. These discrepancies can be addressed by (1) training the model for thermal cycles and (2) enhancing the database in the temperature space to minimize the uncertainty associated with the interpolation of state variables.

APPLICATION: FE SIMULATIONS OF TRANSIENT BEHAVIOR IN PRESSURIZED TUBES

To assess the prospects of using a SM for engineering applications, we simulate the transient response of HT9 tubes. The simulation is based on the work of Cannon et al.,³⁴ which represents realistic reactor conditions. The tiled SM was integrated within the MOOSE finite element framework.⁴⁷ The tube geometry was made similar to that used in Ref. 34 of 5.0 mm inner diameter and 5.8 mm outer diameter. Spherical caps were added on each end of the tubes to avoid the stress concentration in those areas. For the sake of computational efficiency, 2D axisymmetric simulations were performed using geometry schematically shown in Fig. 7a. The tube assembly was meshed with six elements across the thickness, with additional mesh refinement around the tube mid-plane to capture strain localization. The tube was fixed in

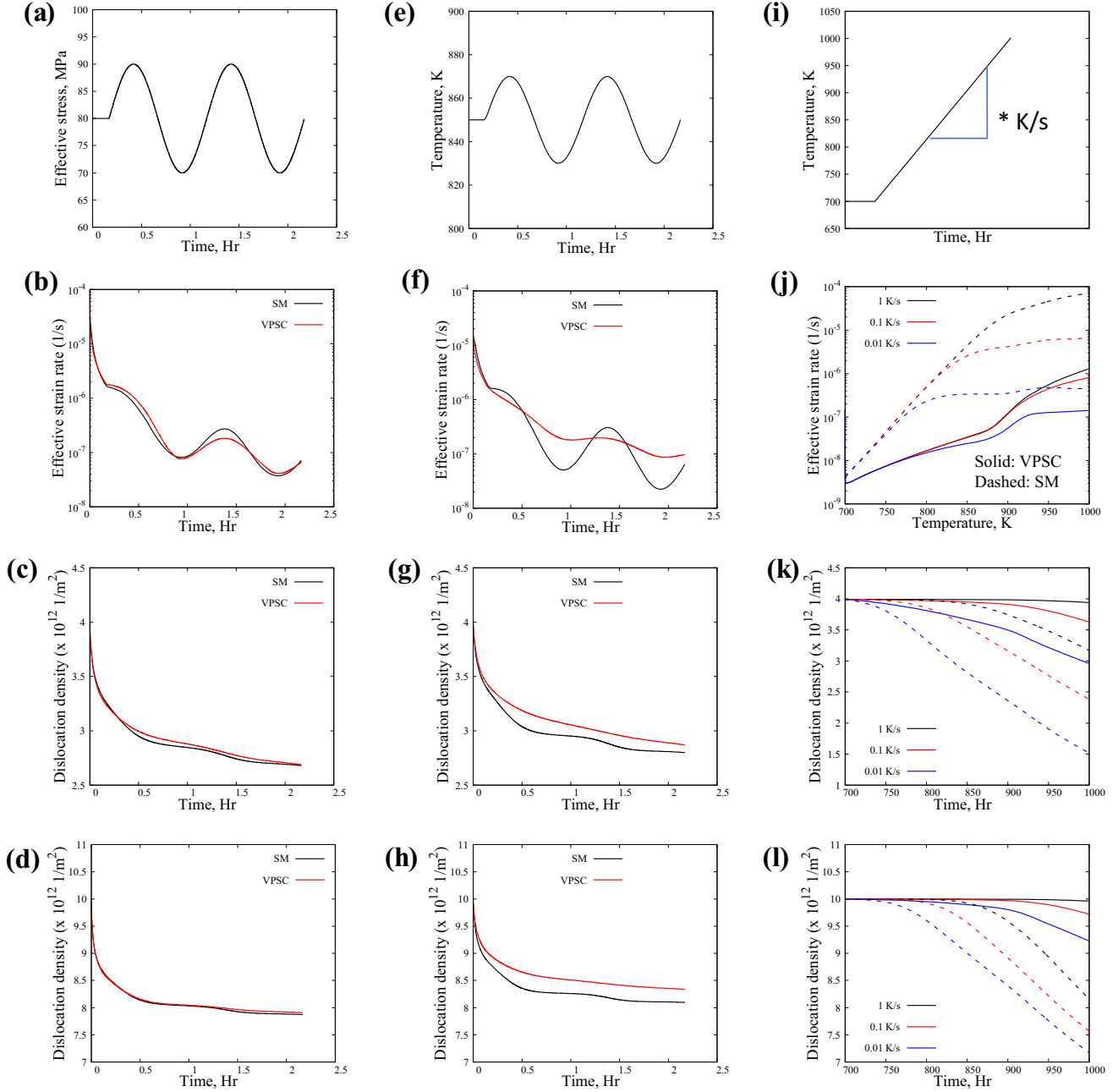


Fig. 6. Assessment of SM predictability against the mechanistic VPSC model for complex loading conditions. Columns correspond to the stress cycle (a–d), temperature cycle (e–h) and temperature ramp (i–l). The first, second, third and fourth rows correspond to the imposed transient condition; the model predicted the effective strain rate, cell and cell wall dislocation densities, respectively. Initial cell and cell wall dislocation densities and the imposed dose rate are $4 \times 10^{12} \text{ m}^{-2}$, $10 \times 10^{12} \text{ m}^{-2}$ and $8 \times 10^{-7} \text{ dpa s}^{-1}$, respectively. In the third column, solid and dashed lines correspond to VPSC and SM models, respectively.

all degrees of freedom at the bottom end of the spherical cap. The top of the cap was allowed to move only along the axial direction.

Two types of transient simulations are performed. First, the tube is subjected to a pressure ramp from 5 MPa to 15 MPa at a rate of 0.01 MPa/s under constant temperature. The temperature distribution along the axial direction of the tube follows the profile shown in Fig. 7b whereby a local increase in

temperature (2%) is maintained midway through the tube. Given the assessments performed in the above, these simulations are expected to be very similar to what one would obtain by embedding VPSC within MOOSE. In a second set of simulations, pressure is maintained constant and the temperature profile is ramped up from 643 K to 1050 K at a rate of 0.56 K/s. These simulations are expected to capture trends but not to be accurate.

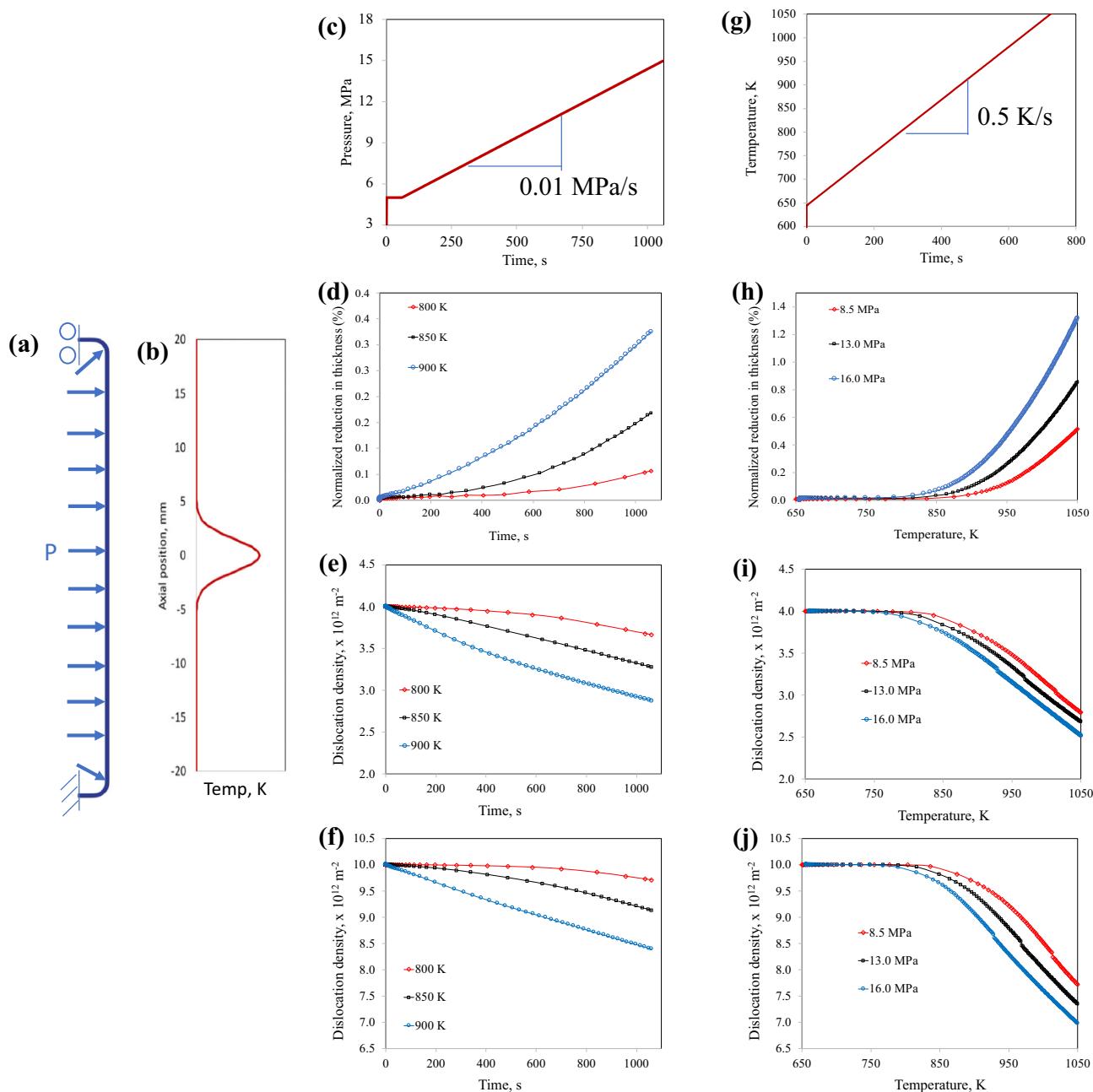


Fig. 7. Transient simulations of a pressurized tube using the developed tiled SM within the MOOSE framework. (a) Schematic representation of the simulation setup of a 2D axis-symmetric tube. (b) Local perturbation in temperature is imposed to localize the failure at the center of the tube. (c) Schematic representation of the imposed pressure ramp from 5 MPa with a rate of 0.01 MPa/s. Model predicted evolution of (d) a normalized reduction in the wall thickness and (e) cell and (f) cell wall dislocation densities, respectively, at the center of the tube for a constant temperatures of 800 K, 850 K and 900 K. (g) Imposed temperature ramp starting from 643 K with a rate of 0.56 K/s. The model calculated the temporal evolution of (h) the reduction tube wall thickness normalized with the initial wall thickness, (i) cell and (j) cell wall dislocation densities at the center of the tube for three different internal pressures: 8.5 MPa, 13 MPa and 16 MPa and 20 MPa.

Internal pressures of 8.5, 13 and 16 MPa were chosen. Initial cell and cell wall dislocation densities were assumed to be 4×10^{12} and 10×10^{12} , respectively. The imposed dose rate was fixed for all the transient cases as $10^{-9} \text{ dpa s}^{-1}$ to approximate the thermal creep conditions.

The MOOSE FE-SM calculations predict the micromechanical fields σ , ε and $\dot{\varepsilon}$ and the evolution of microstructural fields, ρ_{cell} and ρ_{w} , at every element of the tube. For the sake of brevity, only the temporal evolutions of normalized reduction in tube wall thickness and cell and cell-wall dislocation

densities at the center of the tube are shown for both the pressure and temperature ramp cases. Here, the reduction in tube wall thickness is normalized with the initial tube thickness. An increase in the imposed pressure for a constant temperature accelerates the tube thinning due to a rapid increase in the creep rate; see Fig. 7d. Also, the plastic localization induced by the pressure ramp intensifies with an increase in operating temperature. This increase is solely due to the increase in the creep rate as a function of temperature as shown in Fig. 6j. Note that the transients predicted by the model follow from the evolution of the dislocation content; see Fig. 7e and f. Similarly, for the temperature ramp case, the thinning of the tube accelerates with the temperature increase. In addition, the acceleration of tube thinning increases with increasing pressure, which qualitatively agrees with the experimental observations.³⁴ Apart from this, the evolution of tube thinning, i.e., localized deformation, strongly correlates with the evolution of dislocation densities. Overall, these predictions all delineate the SM yield results, which are physical.

CONCLUSION

The present work introduces a computationally efficient, mechanistically informed SM to predict the mechanical response of HT-9 alloy subjected to time-varying stresses, temperatures and irradiation. The approach relied on the generation of a large database of polycrystalline visco-plastic responses populated from a crystal plasticity-based mechanistic constitutive model within the VPSC framework. Interestingly, the entire database is generated from creep simulations under irradiation. Following data reduction, the SM is expressed as a suite of connected tiles each defining the constitutive relationship via the use of polynomial regression. An extensive assessment of the accuracy of the SM was then performed. We reveal first that the SM has high fidelity when used to predict the creep response of HT9 over a wide range of temperatures (600 K to 1100 K), applied stresses (0.1 MPa to 300 MPa) and dpa rates ($1\text{e}-9$ to $1\text{e}-6$ dpa/s). Applications of the SM to transient scenarios (monotonic tension, stress cycling, temperature cycling and temperature ramp) show that although SM was derived from a database of creep response, it performs well when the system is driven by strain or stress. However, this is not the case when the SM is driven by temperature changes. Finally, the SM was integrated into a FE solver which was then used to simulate the transient response of pressurized HT9 tubes. All simulations show that both the pressure and temperature ramp rapidly increase the creep rate and accelerate the thinning of pressurized tubes.

ACKNOWLEDGEMENTS

This work was sponsored by the US Department of Energy, Office of Nuclear Energy, and Nuclear Energy Advanced Modeling and Simulations (NEAMS). This research made use of the resources of the High Performance Computing Center at Idaho National Laboratory, which is supported by the Office of Nuclear Energy of the US Department of Energy and the Nuclear Science User Facilities under Contract No. DE-AC07-05ID14517.

CONFLICT OF INTEREST

On behalf of all the authors, the corresponding author states that there is no conflict of interest.

ELECTRONIC SUPPLEMENTARY MATERIAL

The online version of this article (<https://doi.org/10.1007/s11837-020-04402-2>) contains supplementary material, which is available to authorized users.

REFERENCES

1. A.E. Waltar and A.B. Reynolds, *Fast Breeder Reactors* (Richland: Alan E. Waltar, 1981).
2. T.H. Bauer, G.R. Fenske, and J.M. Kramer, *Cladding Failure Margins for Metallic Fuel in the Integral Fast Reactor* (Lemont: Argonne National Lab, 1987).
3. C.P. Massey, K.A. Terrani, S.N. Dryepondt, and B.A. Pint, *J. Nucl. Mater.* 470, 128 (2016).
4. S. Suman, M.K. Khan, M. Pathak, R.N. Singh, and J.K. Chakravarty, *Nucl. Eng. Des.* 307, 319 (2016).
5. J.M. Kramer, Y.Y. Liu, M.C. Billone, and H.C. Tsai, *J. Nucl. Mater.* 204, 203 (1993).
6. C. Matthews, C. Unal, J. Galloway, D.D.K. Keiser Jr, and S.L. Hayes, *Nucl. Technol.* 198, 231 (2017).
7. J.C. Danko, *Metals Handbook Corrosion*, 9th ed., Vol. 13 (Washington, DC: ASM, 1987).
8. M.O. Speidel and R.M. Magdowski, *Int. J. Press. Vessels Pip.* 34, 119 (1988).
9. W. Wen, A. Kohnert, M. Arul Kumar, L. Capolungo, and C.N. Tomé, *Int. J. Plast* 126, 102633 (2020).
10. F. Garofalo, *Trans. Metall. Soc. AIME* 227, 351 (1963).
11. Y. Estrin and H. Mecking, *Acta Metall.* 32, 57 (1984).
12. H. Mecking and U.F. Kocks, *Acta Metall.* 29, 1865 (1981).
13. W. Wen, L. Capolungo, A. Patra, and C.N. Tomé, *Metall. Mater. Trans. A* 48, 2603 (2017).
14. W. Wen, L. Capolungo, and C.N. Tomé, *Int. J. Plast* 106, 88 (2018).
15. M. Basirat, T. Shrestha, L.L. Barannyk, G.P. Potirniche, and I. Charit, *Metals* 5, 1487 (2015).
16. T.O. Erinosh, K.A. Venkata, M. Mostafavi, D.M. Knowles, and C.E. Truman, *Int. J. Solids Struct.* 139, 129 (2018).
17. B. Chen, D.J. Smith, P.E.J. Flewitt, and M.W. Spindler, *Mater. High Temp.* 28, 155 (2011).
18. J. Segurado, R.A. Lebensohn, J. LLorca, and C.N. Tomé, *Int. J. Plast* 28, 124 (2012).
19. S. Ghosh, *JOM* 67, 129 (2015).
20. S. Keshavarz and S. Ghosh, *Acta Mater.* 61, 6549 (2013).
21. R.A. Lebensohn, A.D. Rollett, and P. Suquet, *JOM* 63, 13 (2011).

22. S. Ghosh, *Micromechanical Analysis and Multi-Scale Modeling Using the Voronoi Cell Finite Element Method* (Boca Raton: CRC Press, 2011).
23. D.L. McDowell, *Handbook of Materials Modeling: Methods: Theory*, Vol. 1 (Berlin: Springer, 2018).
24. D.L. McDowell, *Computational Materials Systems Design* (Berlin: Springer, 2018), pp. 105–146.
25. J.E. Andrade, C.F. Avila, S.A. Hall, N. Lenoir, and G. Vigiani, *J. Mech. Phys. Solids* 59, 237 (2011).
26. F. Feyel and J.-L. Chaboche, *Comput. Methods Appl. Mech. Eng.* 183, 309 (2000).
27. I. Benedetti and F. Barbe, *J. Multiscale Model.* 05, 1350002 (2013).
28. A. Eghtesad, K. Germaschewski, R.A. Lebensohn, and R.A. Knezevic, *Comput. Phys. Commun.* 254, 107231 (2020).
29. A. Eghtesad and M. Knezevic, *J. Mech. Phys. Solids* 134, 103750 (2020).
30. A. Patra and C.N. Tomé, *Nucl. Eng. Des.* 315, 155 (2017).
31. S.R. Kalidindi, H.K. Duvvuru, and M. Knezevic, *Acta Mater.* 54, 1795 (2006).
32. A.E. Tallman, M. Arul Kumar, A. Castillo, W. Wen, L. Capolungo, and C.N. Tomé, *Integr. Mater. Manuf. Innov.* (2020). <https://doi.org/10.1007/s40192-020-00181-5>.
33. C.W. Hunter, R.L. Fish, and J.J. Holmes, *Nucl. Technol.* 27, 376 (1975).
34. N. Cannon, F.-H. Huang, and M. Hamilton, in *STP1046V2-EB 14th Int. Symposium on Effects of Radiation on Materials, Vol. II* (ASTM International, 1990), pp. 729–738.
35. R.A. Lebensohn, C.S. Hartley, C.N. Tomé, and O. Castelnau, *Philos. Mag.* 90, 567 (2010).
36. H. Wang, L. Capolungo, B. Clausen, and C.N. Tomé, *Int. J. Plast* 93, 251 (2017).
37. Y.Q. Wang, M.W. Spindler, C.E. Truman, and D.J. Smith, *Mater. Des.* 95, 656 (2016).
38. P. Franciosi and A. Zaoui, *Acta Metall.* 30, 1627 (1982).
39. U.F. Kocks, A.S. Argon, and M.F. Ashby, *Thermodynamics and Kinetics of Slip* (Oxford: Pergamon Press, 1975).
40. R.L. Coble, *J. Appl. Phys.* 34, 1679 (1963).
41. M.B. Toloczko, B.R. Grambau, F.A. Garner, and K. Abe, in *20th International Symposium on STP1405-EB Effects of Radiation on Materials*. (2001), pp. 557–569.
42. J.L. Deutsch and C.V. Deutsch, *J. Stat. Plan. Inference* 142, 763 (2012).
43. P. Hosemann, S. Kabra, E. Stergar, M.J. Cappillo, and S.A. Maloy, *J. Nucl. Mater.* 403, 7 (2010).
44. H.J. Frost and M.F. Ashby, *Fundamental Aspects of Structure Alloy Design*, ed. R.I. Jaffee and B.A. Wilcox (Boston: Springer, 1977), pp. 27–65.
45. Y. Chen, *Nucl. Eng. Technol.* 45, 311 (2013).
46. S.A. Maloy, T. Romero, M.R. James, and Y. Dai, *J. Nucl. Mater.* 356, 56 (2006).
47. C.J. Permann, D.R. Gaston, D. Andrš, R.W. Carlsen, F. Kong, A.D. Lindsay, J.M. Miller, J.W. Peterson, A.E. Slaughter, R.H. Stogner, and R.C. Martineau, *SoftwareX* 11, 100430 (2020).

Publisher's Note Springer Nature remains neutral with regard to jurisdictional claims in published maps and institutional affiliations.